Modulation of the magnetization and Gilbert damping in Heusler-alloy Co$_{3-x}$Fe$_x$Al thin films

Ruifeng Wang[1], Xingtai Chen[2], Pengfei Yan[1], Yongkang Xu[1], Yilin Zhang[1], Jin Wang[1], Raymond Fan[4], Peter Bencok[4], Paul Steadman[4], Yao Li[1], Wenqin Zou[3], Yongbing Xu[1,5], Ronghua Liu[3,*], Wenqing Liu[2,*] and Liang He[1,*]

[1] Jiangsu Key Laboratory of Advanced Photonic and Electronic Materials, School of Electronic Science and Engineering, Nanjing University, Nanjing 210093, China

[2] Department of Electronic Engineering, Royal Holloway University of London, Egham TW20 0EX, UK

[3] Jiangsu Key Laboratory for Nanotechnology, Department of Physics, Nanjing University, Nanjing 210093, China

[4] Diamond Light Source, Didcot OX11 0DE, UK

[5] Department of Electronic and Physics, University of York, York YO105DD, UK

*Authors to whom correspondence should be addressed: rhliu@nju.edu.cn, wenqing.liu@rhul.ac.uk and heliang@nju.edu.cn

The saturated magnetization (m_{tot}) and the Gilbert damping constant (α) are the two key factors that determine the critical current density of the magnetization reversal in the spin-transfer-torque magnetic memory devices. Here, this study demonstrates the efficient modulation of these two parameters by tunning the composition of the Heusler $Co_{3-x}Fe_xAl$ thin films, utilizing the X-ray magnetic circular dichroism technique and ferromagnetic resonance measurements. With the increase of Fe concentration, the m_{tot} shows a downward trend mainly resulting from the decrease of Fe local magnetic moment instead of Co. On the other hand, the ultralow α decreases from 0.004 to 0.0012. This has been attributed to the reduction of the spin-orbit coupling, which is corroborated by the decrease of the orbit-to-spin moment ratio. Our findings add a building block for the Heusler compounds with tunable Gilbert damping and appropriate magnetization, and show great potential in spintronic applications.

Spintronics is considered a promising solution to utilize the spin of electrons for more efficient information storage and transport in the post-Moore's law era[1, 2]. Ferromagnetic materials, dominating as the core element in spintronic devices, are primarily engineered on the basis of their saturated magnetization[3] and Gilbert damping coefficient[4]. In the spin-torque applications such as magnetic random-access memory (MRAM)[5] and magnetic domain wall motion[6], smaller m_{tot} results in a suppression of the critical current density of magnetization switching[7]. At the same time, lower α reduces the energy dissipation of spin precession and allows magnetization reversal easier[8]. Altogether, it is crucial to modulate both these two key parameters simultaneously for designing high-performance spintronic devices.

Heusler alloys constitute a prominent class of magnetic materials due to the appropriate saturated magnetization, ultralow Gilbert damping constant, high Curie temperature, and predicted half-metallicity. Extensive efforts have been made based on the material engineering during the last few decades[9-11]. Among the studies in Heusler compounds, it has been verified that the saturated magnetization and Gilbert damping can be effectively modulated by simply varying the composition ratio of the internal magnetic elements, such as $Co_{1+x}Fe_{2-x}Si$[12-14], $Co_{3-x}Mn_xSi$[15, 16], and $Co_{2+x}Fe_{1-x}Al$[17, 18] *et al*. However, the spin alignment of the magnetic element species and their role in saturated magnetic moment remain unclear. On the other hand, few reports were attempted to understand the physical mechanism of Gilbert damping using the direct experimental evidence in Co-based Heusler system.

In the present work, we have prepared the single-crystalline Heusler $Co_{3-x}Fe_xAl$

thin films grown on MgO (001) substrates by molecular beam epitaxy (MBE). Element-specific X-ray magnetic circular dichroism (XMCD) technique has clarified that the Co and Fe atoms are ferromagnetically coupled with each other, as well as the decrease in saturated magnetization originates from the reduction of Fe local magnetic moments. Furthermore, we have achieved tunable ultralow Gilbert damping values of 0.0012-0.004 using the ferromagnetic resonance (FMR) measurement. This decrease is strongly dependent on the spin-orbit coupling evidenced experimentally by the orbit-to-spin moment ratios from the XMCD results. This study found that the $CoFe_2Al$ compound with lower magnetization and Gilbert damping is more suitable for the free layer, while the Co_2FeAl film can be utilized as the fixed layer in the MRAM devices.

The 10-nm-thick $Co_{3-x}Fe_xAl$ (x = 1.0 to 2.0) thin films were grown on MgO (001) substrates using MBE technology with a based pressure $< 5\times10^{-10}$ mbar. The atoms were co-evaporated by three K-cell sources. The deposition rates measured by a quartz micro-balance determined the composition ratio. All the films were prepared at the temperature of 275°C, and the real-time growth process was monitored by *in-situ* reflected high energy electron diffraction (RHEED). After the post-annealing, a 2-nm-thick Al layer was deposited to protect the films from oxidation. Then the *B*2 crystal structures were characterized by high resolution X-ray diffraction (HRXRD) [18].

The static hysteresis loops were measured using a vibrating sample magnetometer (VSM), where the external field was applied in the film plane. The dynamic damping properties were obtained by a home-built FMR setup based on a coplanar waveguide (CPW) for microwave field excitation, as shown in the inset of Figure 4(a). The samples

were placed face-down over the CPW center signal line. And the resonance frequency can be tuned from 1 to 20 GHz in this work. The magnetic field was swept parallel to the easy axis [1$\bar{1}$0] direction with a fixed exciting frequency. The X-ray absorption spectroscopy (XAS) and XMCD spectra at Co and Fe absorption edges were measured on the beamline IO10 of the Diamond Light Source in the UK. Circularly polarized X-rays with 100% degree of polarization and a magnetic field of 1.4 T were applied perpendicular to the surface of the thin films. The XAS spectra were obtained using surface-sensitive total electron yield (TEY) detection. Moreover, the XMCD spectra were calculated by taking the difference of XAS spectra $I^+ - I^-$, where I^+ and I^- represent XAS intensity of the left and right helical incoming X-rays, respectively. All the measurements were performed at room temperature.

Figure 1(a) shows the RHEED patterns of Co_2FeAl (left) and $CoFe_2Al$ (right) thin films along the [110] direction. The sharp streaky patterns suggest atomic flat surface morphology for this series. In addition, we have observed the half-streaks marked by the red arrows, i.e., the lower-intensity peaks positioning at $(0\ \frac{1}{2})$ or $(0\ -\frac{1}{2})$, which are attributed to the surface reconstruction which means the perfectly flat surface, indicating the high crystal quality of the films[10]. As shown in Figure 1(b), the Co_2FeAl compounds (left) crystallize in the regular Heusler structure, while the $CoFe_2Al$ alloys (right) belong to the inverse Heusler structure where half of the Co atoms on the 8c Wyckoff sites are replaced by the Fe(4d) atoms. Figure 1(c) shows that square hysteresis loops measured by VSM reveal the in-plane magnetic anisotropy for all the $Co_{3-x}Fe_xAl$ films. The small coercivity H_C suggests the soft ferromagnetic property[18].

And the specific values of the saturated magnetization are summarized in Table 1, which are consistent with previous reported data[19].
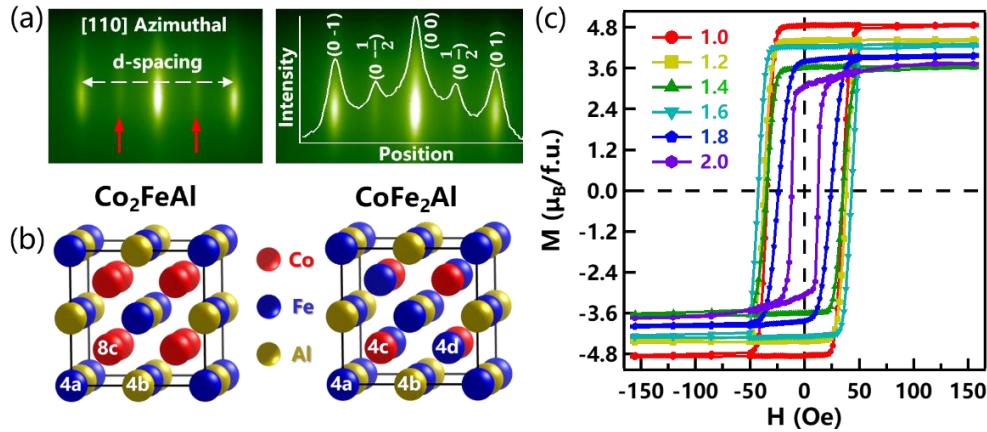

Figure 1 RHEED patterns and hysteresis loops of $Co_{3-x}Fe_xAl$ films. (a) The RHEED patterns of Co_2FeAl (left) and $CoFe_2Al$ (right) films. The RHEED intensity versus position is shown for $CoFe_2Al$ sample. The incident electron beam is along azimuths [110] direction. (b) The Crystal structure of Co_2FeAl (left) and $CoFe_2Al$ (right), the atoms are labelled by the corresponding Wyckoff positions. (c) The hysteresis loops with the magnetic field applied parallel to the [110] axis at room temperature.

Figure 2(a) illustrates the geometry of the XMCD measurement. A typical XAS and XMCD spectra of Co and Fe $L_{2,3}$ edges for this series are presented in Figure 2(b) and 2(c), respectively. The XAS spectra present two main absorption peaks corresponding to the L_2 and L_3 edges derived from the excitations from $2p_{1/2}$ and $2p_{3/2}$ sub-levels[20], respectively. The distinct metallic peaks of XAS spectra without multiplet structures for both left and right circularly polarized X-rays indicate that the samples

were not oxidized atomically[19, 21]. For all the samples, a shoulder structure[19, 20, 22] highlighted by the grey arrow has been observed in the higher photon energy region (about 3 eV) of the Co L_3 edge due to the photoelectron scattering from the ordered lattice. This case also suggests the high ordering with the $B2$ phase structure[19], which agrees with the XRD results. The XMCD spectra obtained by taking the difference of XAS spectra are shown in the bottom panel of Figure 2(b) and 2(c). From the XMCD spectra, the same sign between Co and Fe $L_{2,3}$ edges suggests that the magnetic moment of both Co and Fe elements are ferromagnetically coupled.
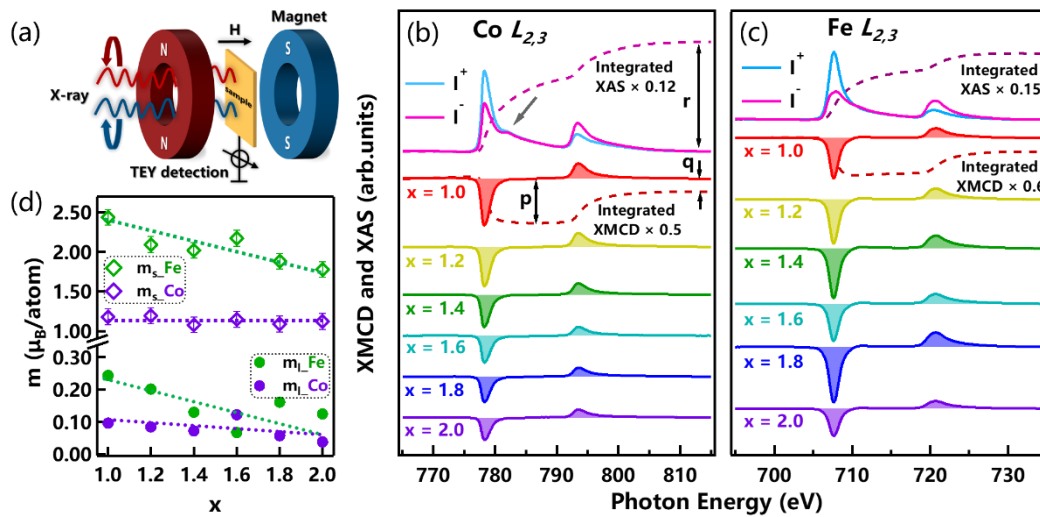

Figure 2 Room temperature XAS and XMCD results of Co and Fe for $Co_{3-x}Fe_xAl$ films. (a) Schematic diagram of XMCD experimental setup. Typical pairs of XAS and XMCD spectra of Co (b) and Fe (c) and their integrals (the XMCD spectra are offset vertically for clarity). I^+ and I^- stand for the XAS spectra measured by the left and right X-ray helicities, respectively. The dash lines indicate the integration of the spectra. (d) Spin magnetic moment m_s (top) and orbital magnetic moment m_l (bottom) of different atoms versus Fe compositions. The m_l of Co and Fe atom overall

shows a downward trend. The m_s of Fe decreases with the increasing x while the m_s of Co remains constant.

To quantitatively address the average magnetic moments, the magneto-optical sum rules[23] neglecting the magnetic diploe operator are adopted to analyze the XAS and XMCD spectra. Here, the spin (m_s) and orbital (m_l) magnetic moments of Co and Fe atoms can be calculated by the following equations[21]

$$m_l = -\frac{4qn_h}{3rP\cos\theta} \tag{1}$$

$$m_s = -\frac{(6p-4q)n_h}{rP\cos\theta} \tag{2}$$

where the parameter p is the L_3 edge integrated intensity of XMCD spectra, $p = \int_{L_3}(I^+ - I^-)dE$. q is the XMCD integral over the $L_{2,3}$ edges, and $q = \int_{L_2+L_3}(I^+ - I^-)dE$. r is the sum of the $L_{2,3}$ edges integrated intensity of XAS spectra, expressed as $r = \int_{L_2+L_3}(I^+ + I^-)dE$. P and θ denote the circular polarization ratio of the X-ray and the angle from the normal to the sample surface. Here $P = 100\%$ and $\theta = 0°$ for our measurement. n_h is the effective number of valence holes obtained by integrating over the unoccupied density of $3d$ states, and is assumed to be 2.5 for Co and 3.4 for Fe[19], respectively. An arctangent-based step function was introduced to exclude the nonmagnetic influence of the XAS spectra[24]. As shown in Figure 2(b) and 2(c), the flat integration of both XAS and XMCD spectra (dashed line) provide a proper background offset[25].

Utilizing the sum rules, Figure 2(d) presents the Fe composition dependence of the deduced effective orbital (m_l) and spin (m_s) moments of Co and Fe atoms. Regarding

the spin moments, it should be noted that the m_s is about one order of magnitude larger than the m_l for all the films. The m_s of Fe atom decreases with the increase of Fe composition while that of Co atom is relatively constant. The non-zero orbital moments suggest the existence of spin-orbit coupling[26] and show a decreasing trend with increasing Fe concentrations. The orbital moment strongly depends upon the electronic occupied states near the Fermi level[26]. The m_l equals zero for the fully filled or empty spin bands, while the m_l can reach a maximum for a half-filled spin-down band[26]. The m_l of Fe atom is larger, since the electronic occupied state of Fe atom ($3d^6$) is close to the half-filled states ($3d^5$) comparing with the state of Co atom ($3d^7$). Additionally, the local magnetic moments of Co and Fe atoms in the Co_2FeAl sample are close to those values investigated by Zhang et al[19].

Figure 3(a) shows the total magnetic moments (m_{tot}) determined by the XMCD technology and VSM measurement for all the samples. For this series, the nearest-neighbor Co(8c)-Fe(4a) exchange interaction plays a dominant role in magnetic moments[19], while another nearest-neighbor Fe(4d)-Fe(4a) exchange interaction does not influence the magnetic moment remarkably[27]. As the Co(8c) atoms are consecutively substituted by Fe(4d) atoms with increasing x, Co(8c)-Fe(4a) exchange interaction gradually reduces due to the decrease of Co(8c) atoms. Hence, the total magnetic moments overall decline with the increasing Fe composition. And the upward behavior between x = 1.4 - 1.6 may be attributed to the structural transition[18] from regular to inverse Heusler structure. Moreover, the experimental data obey the Slater-Pauling curve[12] (Green line), which describes the linear dependence of the m_{tot} on the

total valence electron numbers N_v. For full Heusler alloys, this relation is usually given by the equation: $m_{tot} = N_v - 24$. The m_{tot} deduced by XMCD method follows this equation in the Co-rich region but has slightly higher values in the Fe-rich region. Similar cases have also been reported previously for the $Co_{1+x}Fe_{2-x}Si$ Heusler compounds[12]. This deviation may be attributed to the additional next-nearest-neighbor Co(8c)-Fe(4d) exchange interaction in the Fe-rich region, since only inverse Heusler structure could stimulate this exchange interaction due to enough Fe(4d) atoms. In addition, this upward behavior may be also ascribed to the other factors including local disorder, spin-orbit coupling, weak localization, and local exchange interactions[18].
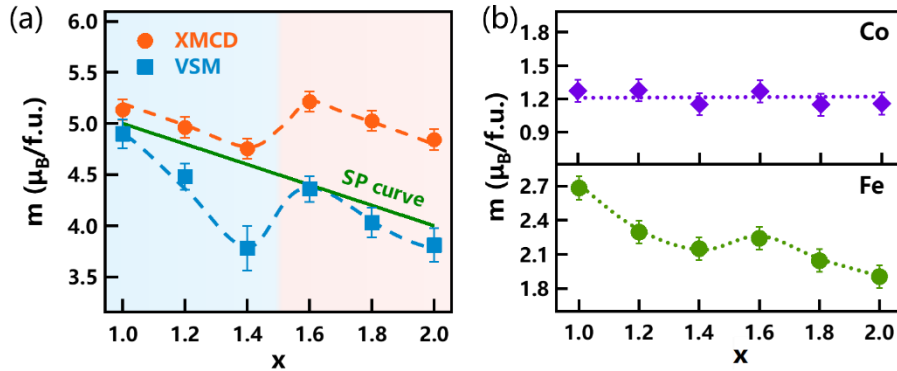

Figure 3 Magnetic properties for $Co_{3-x}Fe_xAl$ films. (a) The total magnetic moment m_{tot} from VSM and XMCD as a function of Fe concentration x. All the m_{tot} show downward trend overall and have a kink between the intermediate compositions. (b) The local magnetic moment of Co atoms (top) and Fe atoms (bottom) versus x. The m_{Co} remain constant while the m_{Fe} have a drastically decrease with the increasing x.

Furthermore, the m_{tot} measured by VSM is slightly lower than those by XMCD,

which is attributed to the weaker magnetization layer at the interface between the sample and MgO substrate[19]. In other words, the VSM measures the average magnetic moment of the whole film. In comparison, the XMCD intensity generally obtains signals from the top few layers[24, 25]. Hence, the magnetic moments from XMCD are bulk-like for our samples. For the Co_2FeAl sample, the total magnetic moment of 5.13 ± 0.10 μ_B/f.u. (XMCD) is reasonably close to the theoretical bulk value of 5.00 μ_B/f.u. [27]. For the $CoFe_2Al$ film, the observed m_{tot} of 4.86 ± 0.10 μ_B/f.u. (XMCD) is also consistent with the reported[27] bulk value of 4.91 μ_B/f.u.

To further study the magnetic moment contribution of Co and Fe atoms for this series, the XMCD data were used to estimate the local magnetic moments. As shown at the top of Figure 3(b), m_{Co} is nearly constant, which is possibly due to the unchanged nearest-neighbor environment of Co atoms[12]. The estimated local moments of $(1.16\text{-}1.28) \pm 0.10$ μ_B/atom for Co atoms are in reasonable agreement with experimental (1.21 μ_B/atom)[28] and theoretical data (1.29 μ_B/atom)[27].

It is noted that the XMCD measurement cannot distinguish the local magnetic moment of specific Fe atoms at different sites. Thus, the local Fe moments are the average atomic moment of all the Fe atoms in our work. Figure 3(b) (bottom) demonstrates that m_{Fe} overall exhibits a downward trend with the increasing Fe composition, which is also attributed to the reduction of Fe(4a)-Co(4c) exchange interaction since the Co(4c) atoms decrease. Besides, the calculated m_{Fe} of 2.68 ± 0.10 μ_B/atom and 1.90 ± 0.10 μ_B/atom for Co_2FeAl and $CoFe_2Al$ are close to the reported values of 2.64 μ_B/atom[19] and 2.15 μ_B/atom[27], respectively. As suggested by the

magnetic moments of Co and Fe atoms, the decrease of total magnetic moments in the two regions primarily originates from the decrease of the Fe local magnetic moments. This conclusion is utterly different from the report on the variation of total magnetic moments in the bulk $Co_{1+x}Fe_{2-x}Si$, which originates from the local magnetic moment of Co atoms[12].

Apart from the saturated magnetization, Gilbert damping constants were investigated utilizing FMR measurement. Figure 4(a) shows the typical FMR absorption spectra for the $Co_{3-x}Fe_xAl$ films at the frequency of 10 GHz , which can be well fitted by a sum of symmetric and anti-symmetric Lorentzian derivatives[29]

$$\frac{dP}{dH}(H) = L\frac{\Delta H(H-H_r)}{[(H-H_r)^2+\Delta H^2]^2} + D\frac{\Delta H^2-(H-H_r)^2}{[(H-H_r)^2+\Delta H^2]^2} \qquad (3)$$

where H_r and ΔH represent the resonance field and the linewidth, respectively. L and D are the symmetric and antisymmetric fitting parameters of the FMR spectra, respectively. The data were offset for clarity. A significant shift of resonance field to higher fields (the pink dashed line) was observed with the increasing Fe composition x. In addition, it is notable that a perpendicular standing spin wave mode[30] appears at a lower magnetic field for the sample with $x = 1.8$, which may be due to the surface partial spin pinning affected by the anisotropy field[31, 32].

Figure 4(b) shows the frequency dependence of resonance filed H_r for all the samples. The data can be well fitted by the Kittel equation[29]

$$f = \frac{\gamma}{2\pi}\sqrt{(H_r - H_K)(H_r - H_K + 4\pi M_{eff})} \qquad (4)$$

where the γ $(=g\mu_B/\hbar)$ is the gyromagnetic ratio and g is the Landé g factor, μ_B is the Bohr magneton, and $\hbar$ is the reduced Planck constant. $4\pi M_{eff}$ is the effective

saturation magnetization and H_K is the in-plane anisotropy field. The g value approaching to 2 suggests that the magnetic moment mainly arises from the spin moment contribution[33].
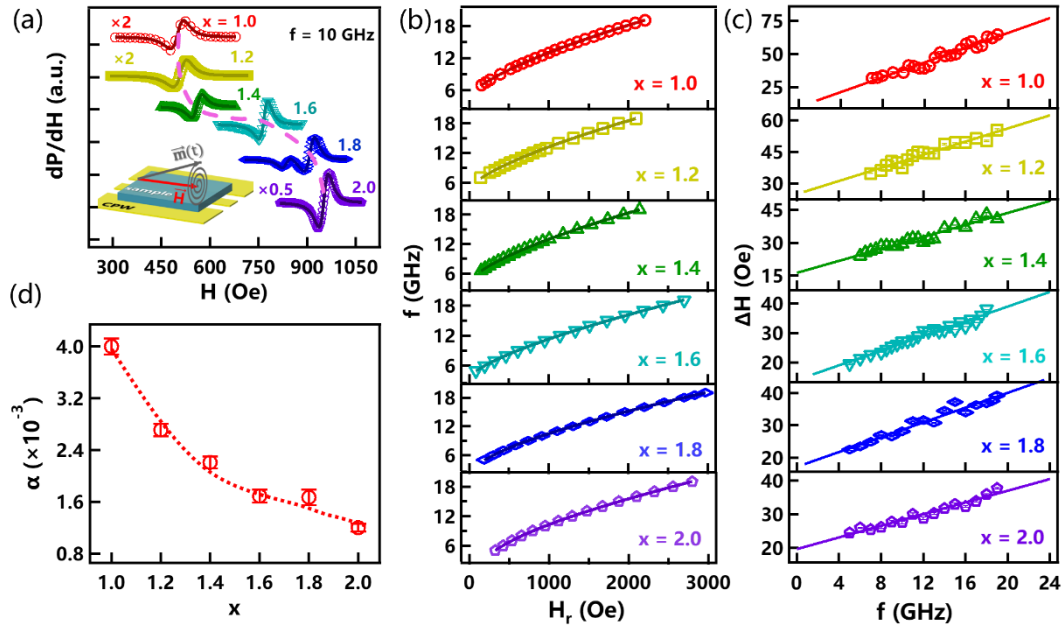

Figure 4 Room temperature FMR analysis for Co$_{3-x}$Fe$_x$Al films. (a) Magnetic field dependence of the amplitude of FMR spectra at $f = 10$ GHz. The inset is a schematic of the CPW-based FMR measurement. (b) Frequency versus resonance field H_r for various Fe composition. The solid lines are fits to the data using the Kittle equation. (c) Frequency dependent FMR linewidth ΔH. The solid lines are linear fits to the data. (d) Fe composition dependent Gilbert damping constant α. The α show a consecutive downward trend.

Figure 4(c) reveals that the FMR linewidth increases linearly with the frequency for all the samples. The Gilbert damping constant can be estimated by fitting the frequency-dependent linewidth[34]

$$\Delta H = \frac{4\pi f}{\gamma}\alpha + \Delta H_0 + \Delta H_{TMS} \tag{5}$$

where α is the Gilbert damping constant. The ΔH_0 represents the inhomogeneous broadening. The ΔH_{TMS} is the extrinsic two-magnon scattering (TMS) broadening. The TMS contribution is negligible in our work, since the linear frequency dependence of the ΔH covers the entire frequency range, which is substantially different from the nonlinear behavior (convex) caused by the TMS[35-37]. The obtained Gilbert damping constants steadily decrease by 70% from 0.004 (x = 1.0) to 0.0012 (x = 2.0) with the increasing Fe concentration *x*, as shown in Figure 4(d). These Gilbert damping constants are comparable with the lowest value of 0.001 ever reported in a 50-nm-thick Co_2FeAl film[38].

Kambersky's torque-correlation model predicts that the Gilbert damping mainly dependents on the density of states at Fermi level ($N(E_F)$) or the spin-orbit coupling (SOC). To gain an insight into the origin of the Gilbert damping, we calculated the $N(E_F)$ using the first-principles calculation and investigated the SOC described by the orbit-to-spin moment ratio (m_l/m_s) [26, 34, 39, 40]. The inconsistent composition dependence of $N(E_F)$ and the Gilbert damping suggests that the $N(E_F)$ is not the dominate factor for the decrease of Gilbert damping, as shown in Supplementary Information. Indeed, the ratios m_l/m_s decreases from 0.098 to 0.055 with the increasing *x*. As shown in Figure 5, the Gilbert damping constant α and the ratio m_l/m_s have a strong positive correlation with each other, suggesting that the reduction of the Gilbert damping mainly originates from the decrease of the spin-orbit coupling.
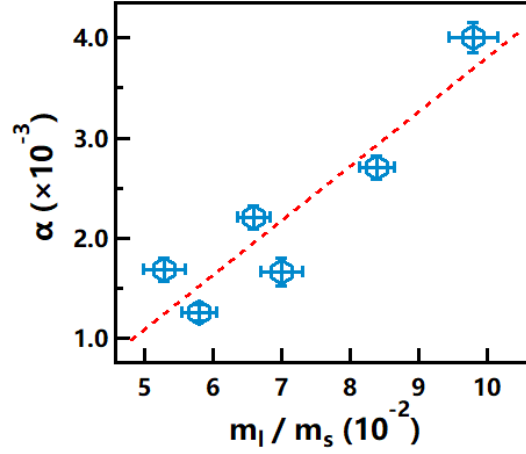
Figure 5 The Gilbert damping constant α versus orbit-spin moment ratio m_l/m_s in the $Co_{3-x}Fe_xAl$

series.

Table 1 Magnetic moment results from the XMCD and VSM measurements on $Co_{3-x}Fe_xAl$ related

to the Fe composition x and the number of valence electrons N_v. The magnetic moments including

local magnetic moments of Co (m_{Co}, unit: μ_B/atom) and Fe (m_{Fe}, unit: μ_B/atom) atoms and spin

moments (m_s, unit: μ_B/atom) have an error of ± 0.10 μ_B. The error of orbital moment (m_l, unit:

μ_B/atom) is ± 0.01 μ_B.

Sample		XMCD						VSM
x	N_v	m_{Co}	m_{Fe}	m_l	m_s	m_l/m_s ($\times 10^{-2}$)	m_{tot} (μ_B/f.u.)	M (μ_B/f.u.)
1.0	29.0	1.28	2.68	0.15	1.60	9.8	5.14	4.90 ± 0.14
1.2	28.8	1.28	2.30	0.13	1.55	8.4	4.96	4.48 ± 0.13
1.4	28.6	1.16	2.15	0.10	1.52	6.6	4.76	3.80 ± 0.20
1.6	28.4	1.27	2.24	0.09	1.69	5.5	5.26	4.36 ± 0.13
1.8	28.2	1.17	2.04	0.11	1.57	7.0	4.96	4.03 ± 0.14
2.0	28.0	1.18	1.90	0.09	1.56	5.8	4.87	3.81 ± 0.16

In summary, the Heusler-alloy $Co_{3-x}Fe_xAl$ thin films have been deposited on MgO

(001) substrates. The saturated magnetic moments measured by the VSM and XMCD

techniques demonstrate similar downward trends with increasing Fe concentration, which overall obeys the classical Slater-Pauling curve in the Full-Heusler compounds. We clarified that the Co and Fe atoms are ferromagnetically coupled. The nearly unchanged m_{Co} and drastically decreasing m_{Fe} indicated that the tunable total magnetic moments m_{tot} mainly results from the variation of the Fe local magnetic moments. The ultralow Gilbert damping constants have been modulated from 0.004 to 0.0012 with the increasing Fe composition in this series. Furthermore, the reduction of the α is attributed to the decrease of the spin-orbit coupling represented by the ratio m_l/m_s. These results shed light on the tunability and fundamental mechanism of the magnetic properties in Heusler alloy, which helps explore advanced spintronic devices.

AUTHOR'S CONTRIBUTIONS

R. Wang and X. Chen contributed equally to this work.

SUPPLEMENTARY MATERIAL

See the supplementary material for the RHEED patterns, the XAS spectra and the DOS at Fermi level of the $Co_{3-x}Fe_xAl$ samples.

ACKNOWLEDGMENTS

References

[1] L. Guo, X. Gu, X. Zhu, and X. Sun, Adv. Mater. **31**, 1805355 (2019).

[2] S. Peng, D. Zhu, J. Zhou, B. Zhang, A. Cao, M. Wang, W. Cai, K. Cao, and W. Zhao, Adv. Electron. Mater. **5**, 1900134 (2019).

[3] K. Wang, Z. Xu, F. Ling, Y. Wang, and S. Dong, Appl. Surf. Sci. **435**, 1125 (2018).

[4] A. Brataas, Y. Tserkovnyak, and G.E. Bauer, Phys. Rev. Lett. **101**, 037207 (2008).

[5] M. Belmeguenai, F. Zighem, Y. Roussigné, S.M. Chérif, P. Moch, K. Westerholt, G. Woltersdorf, and G. Bayreuther, Phys. Rev. B **79**, 024419 (2009).

[6] Z. Luo, A. Hrabec, T.P. Dao, G. Sala, S. Finizio, J. Feng, S. Mayr, J. Raabe, P. Gambardella, and L.J. Heyderman, Nature **579**, 214 (2020).

[7] C. Luo, Z. Feng, Y. Fu, W. Zhang, P.K.J. Wong, Z.X. Kou, Y. Zhai, H.F. Ding, M. Farle, J. Du, and H.R. Zhai, Phys. Rev. B **89**, 184412 (2014).

[8] S. Sakamoto, T. Higo, S. Tamaru, H. Kubota, K. Yakushiji, S. Nakatsuji, and S. Miwa, Phys. Rev. B **103**, 165122 (2021).

[9] C. Guillemard, S. Petit-Watelot, J.C. Rojas-Sánchez, J. Hohlfeld, J. Ghanbaja, A. Bataille, P. Le Fèvre, F. Bertran, and S. Andrieu, Appl. Phys. Lett. **115**, 172401 (2019).

[10] C. Guillemard, W. Zhang, G. Malinowski, C. de Melo, J. Gorchon, S. Petit-Watelot, J. Ghanbaja, S. Mangin, P. Le Fevre, F. Bertran, and S. Andrieu, Adv. Mater. **32**, 1908357 (2020).

[11] T. Li, W. Yan, X. Zhang, B. Hu, K. Moges, T. Uemura, M. Yamamoto, M. Tsujikawa, M. Shirai, and Y. Miura, Phys. Rev. B **101**, 174410 (2020).

[12] J.E. Fischer, J. Karel, S. Fabbrici, P. Adler, S. Ouardi, G.H. Fecher, F. Albertini, and C. Felser, Phys. Rev. B **94**, 024418 (2016).

[13] K. Srinivas, T. Prasanna Kumari, M. Manivel Raja, and S.V. Kamat, J. Appl. Phys. **114**, 033911 (2013).

[14] C. Sterwerf, S. Paul, B. Khodadadi, M. Meinert, J.-M. Schmalhorst, M. Buchmeier, C.K.A. Mewes, T. Mewes, and G. Reiss, J. Appl. Phys. **120**, 083904 (2016).

[15] M. Oogane, A.P. McFadden, K. Fukuda, M. Tsunoda, Y. Ando, and C.J. Palmstrøm, Appl. Phys. Lett. **112**, 262407 (2018).

[16] S. Andrieu, A. Neggache, T. Hauet, T. Devolder, A. Hallal, M. Chshiev, A.M. Bataille, P. Le Fèvre, and F. Bertran, Phys. Rev. B **93**, 094417 (2016).

17. Z. Chen, X. Ruan, B. Liu, L. Yang, J. Wu, C. Gao, H. Meng, L. He, R. Zhang, and Y. Xu, J. Phys.: Condens. Mat. **31**, 075802 (2019).

18. R. Wang, Q. Gao, R. Liu, Y. Zhao, J. Ning, P. Yan, Y. Sun, J. Wang, Q. Zeng, J. Du, Y. Xu, and L. He, J. Phys. D: Appl. Phys. **55**, 395002 (2022).

19. X. Zhang, W. Liu, Y. Yan, W. Niu, B. Lai, Y. Zhao, W. Wang, L. He, H. Meng, and Y. Xu, Appl. Phys. Lett. **113**, 212401 (2018).

20. S. Soni, S. Dalela, S.S. Sharma, E.K. Liu, W.H. Wang, G.H. Wu, M. Kumar, and K.B. Garg, J. Alloys. Compd. **674**, 295 (2016).

21. Z. Chen, W. Liu, P. Chen, X. Ruan, J. Sun, R. Liu, C. Gao, J. Du, B. Liu, H. Meng, R. Zhang, and Y. Xu, Appl. Phys. Lett. **117**, 012401 (2020).

22. P. Klaer, B. Balke, V. Alijani, J. Winterlik, G.H. Fecher, C. Felser, and H.J. Elmers, Phys. Rev. B **84**, 144413 (2011).

23. S. Sakamoto, T. Higo, M. Shiga, K. Amemiya, S. Nakatsuji, and S. Miwa, Phys. Rev. B **104** (2021).

24. Liu W., Xu Y., He L., Laan G., Zhang R., and W. K., Sci. Adv. **5**, eaav2088 (2019).

25. X. Zhang, Q. Lu, W. Liu, W. Niu, J. Sun, J. Cook, M. Vaninger, P.F. Miceli, D.J. Singh, S.W. Lian, T.R. Chang, X. He, J. Du, L. He, R. Zhang, G. Bian, and Y. Xu, Nat. Commun. **12**, 2492 (2021).

26. W. Zhang, D. Zhang, P.K. Wong, H. Yuan, S. Jiang, G. van der Laan, Y. Zhai, and Z. Lu, ACS Appl. Mater. Interfaces **7**, 17070 (2015).

27. L. Siakeng, G.M. Mikhailov, and D.P. Rai, J. Mater. Chem. C **6**, 10341 (2018).

28. J. Okabayashi, H. Sukegawa, Z. Wen, K. Inomata, and S. Mitani, Appl. Phys. Lett. **103** (2013).

29. L. Bainsla, A. Kumar, A.A. Awad, C. Wang, M. Zahedinejad, N. Behera, H. Fulara, R. Khymyn, A. Houshang, J. Weissenrieder, and J. Åkerman, Adv. Funct. Mater. **32**, 2111693 (2022).

30. Y. Yin, M. Ahlberg, P. Durrenfeld, Y. Zhai, R.K. Dumas, and J. Akerman, IEEE Magn. Lett. **8**, 3502604 (2017).

31. B. Samantaray, A.K. Singh, C. Banerjee, A. Barman, A. Perumal, and P. Mandal, IEEE T. Magn. **52**, 1 (2016).

32. A. Krysztofik, H. Głowiński, P. Kuświk, S. Ziętek, L.E. Coy, J.N. Rychły, S. Jurga, T.W. Stobiecki, and J. Dubowik, J. Phys. D: Appl. Phys. **50**, 235004 (2017).

[33] H.T. Nembach, T.J. Silva, J.M. Shaw, M.L. Schneider, M.J. Carey, S. Maat, and J.R. Childress, Phys. Rev. B **84**, 054424 (2011).

[34] Z. Huang, W. Liu, J. Yue, Q. Zhou, W. Zhang, Y. Lu, Y. Sui, Y. Zhai, Q. Chen, S. Dong, J. Wang, Y. Xu, and B. Wang, ACS Appl. Mater. Interfaces **8**, 27353 (2016).

[35] W.K. Peria, T.A. Peterson, A.P. McFadden, T. Qu, C. Liu, C.J. Palmstrøm, and P.A. Crowell, Phys. Rev. B **101**, 134430 (2020).

[36] K. Lenz, H. Wende, W. Kuch, K. Baberschke, K. Nagy, and A. Jánossy, Phys. Rev. B **73**, 144424 (2006).

[37] L. Chen, S. Mankovsky, S. Wimmer, M.A.W. Schoen, H.S. Körner, M. Kronseder, D. Schuh, D. Bougeard, H. Ebert, D. Weiss, and C.H. Back, Nat. Phys. **14**, 490 (2018).

[38] S. Mizukami, D. Watanabe, M. Oogane, Y. Ando, Y. Miura, M. Shirai, and T. Miyazaki, J. Appl. Phys. **105**, 07D306 (2009).

[39] Z. Zhang, E. Liu, X. Lu, W. Zhang, Y. You, G. Xu, Z. Xu, P.K.J. Wong, Y. Wang, B. Liu, X. Yu, J. Wu, Y. Xu, A.T.S. Wee, and F. Xu, Adv. Funct. Mater. **31** (2021).

[40] G.D. Hwee Wong, Z. Xu, W. Gan, C.C.I. Ang, W.C. Law, J. Tang, W. Zhang, P.K.J. Wong, X. Yu, F. Xu, A.T.S. Wee, C.S. Seet, and W.S. Lew, ACS Nano **15**, 8319 (2021).